Numerical simulation of localization phenomena using gradient plasticity and finite elements

Jerzy Pamin
Delft University of Technology, Faculty of Civil Engineering
Presently back at Cracow University of Technology, Faculty of Civil Engineering

René de Borst
Delft University of Technology, Faculty of Civil Engineering
Also at Eindhoven University of Technology, Faculty of Mechanical Engineering

A gradient plasticity theory is proposed, which includes dependence of the yield function on the Laplacian of an invariant plastic strain measure. The theory preserves well-posedness of the governing equations in the presence of strain softening and prevents the pathological mesh sensitivity of numerical results. An internal length scale incorporated in the theory determines the size of localization bands. Adopting a weak satisfaction of the yield condition, mixed finite elements are developed, in which plastic strains are discretized in addition to the standard discretization of the displacements. A gradient-dependent Drucker-Prager yield function is used to solve a two-dimensional problem of shear slip in a soil mass. A gradient-dependent Rankine failure function is used in continuum modelling of two concrete fracture experiments. The regularizing effect of the gradient dependence is demonstrated.

Keywords: Softening, strain localization, higher-order continuum, finite element analysis, soil instability, concrete fracture.

Introduction

Conventional constitutive models with strain softening exhibit a pathological mesh sensitivity of numerical results. The size of the localization zone is completely determined by the discretization and the direction of the localization band may be biased by the mesh lines. The reason for this behaviour is the fact, that the boundary value problem easily ceases to be well-posed at the onset of strain softening, which is a material instability. The standard continuum equations then predict localization of deformation in a set of measure zero (a line in 2D configurations) and a finite element solution attempts to reproduce this result by a localization band that is one or two elements wide in decohesion or shear slip problems, respectively.

Various approaches have been suggested to remove the ill-posedness of the governing equations, cf. Willam et al. (1992), Sluys (1992), de Borst et al. (1993). In this paper a higher-order continuum approach called gradient plasticity is used as a regularization method, cf. Aifantis (1984), Zbib et al. (1988), Mühlhaus et al. (1991), Vardoulakis et al. (1991), de Borst et al. (1992). In this approach the

yield function depends on the second order spatial derivatives of an invariant plastic strain measure. This dependence preserves ellipticity of the equilibrium equations during localization and introduces an internal length scale defining the width of the localization band. From the physical viewpoint, we can associate the higher-order gradients in the macroscopic constitutive model with the nonlocal interaction between microstructural deformation carriers.

Due to the gradient dependence of the yield function the consistency condition, which governs the plastic flow, is a partial differential equation. Therefore the determination of the plastic multiplier is not as simple as in classical plasticity. It has been proposed, Mühlhaus et al. (1991), de Borst et al. (1992), to satisfy the consistency equation in a distributed sense and to discretize the plastic strain field in addition to the usual discretization of the displacements. A general formulation and a solution algorithm for the gradient-dependent plasticity theory have been presented by de Borst et al. (1992). This paper presents the possible finite element formulations of the problem together with some applications to soil instability and concrete fracture problems in two dimensions, cf. Pamin (1994).

In this paper we limit the consideration to static problems with a monotonic loading and small deformations of the analyzed configurations. We employ a deterministic description of an isotropic and homogeneous continuum. The theory of gradient-dependent plasticity is summarized in Section 2 together with the incremental equations, which are the starting point of the derivation of different finite elements, presented in Section 3.

The performance of the gradient plasticity theory and some finite elements are investigated in Sections 4-5. Simulations of a slope stability problem in a soil mass under plane strain conditions are described in Section 4 using the gradient-dependent Drucker-Prager yield function with linear cohesion softening. Fracture of a Single-Edge-Notched (SEN) beam, Schlangen (1993), and a Double-Edge-Notched (DEN) specimen, Nooru-Mohamed (1992), is numerically predicted in Section 5 by means of the Rankine failure function with a nonlinear gradient-dependent softening rule. Section 6 includes some final remarks.

Gradient-dependent plasticity

Rate boundary value problem

Firstly, we summarize the rate boundary value problem of gradient plasticity, cf. de Borst et al. (1992), Pamin (1994). We introduce the displacement vector $\mathbf{u} = (u_x, u_y, u_z)$, the strain tensor in a vector form $\varepsilon = (\varepsilon_{xx}, \varepsilon_{yy}, \varepsilon_{zz}, \gamma_{xy}, \gamma_{yz}, \gamma_{zx})$ and the stress tensor in a vector form $\sigma = (\sigma_{xx}, \sigma_{yy}, \sigma_{zz}, \sigma_{xy}, \sigma_{yz}, \sigma_{zx})$. Under the assumption of small deformations and static loading we have the following equations for an elasto-plastic body occupying a volume V:

$$\mathbf{L}^T \dot{\sigma} + \dot{\mathbf{b}} = 0, \tag{1}$$

$$\dot{\varepsilon} = \mathbf{L}\dot{\mathbf{u}}, \tag{2}$$

$$\dot{\sigma} = \mathbf{D}^e (\dot{\varepsilon} - \dot{\lambda}\mathbf{m}) \tag{3}$$

where superimposed dots denote the derivative with respect to time and the superscript T is the transpose symbol. In the above equations $\mathbf{L}$ is a differential operator matrix, $\mathbf{b}$ is a body-force vector

and $\mathbf{D}^e$ is the elastic stiffness matrix. Eq. (3) contains the definition of the plastic strain-rate vector, called the flow rule:

$$\dot{\varepsilon}^P = \lambda \mathbf{m}, \quad \mathbf{m} = \frac{\partial G}{\partial \sigma} \tag{4}$$

in which λ is a plastic multiplier and $\mathbf{m}$ defines the direction of the plastic flow. The vector $\mathbf{m}$ may be derived from a plastic potential function G.

The gradient dependence is included solely in the definition of the yield function F

$$F = F(\sigma, \kappa, \nabla^2 \kappa), \tag{5}$$

in which κ is an invariant plastic strain measure (the hardening parameter). Together with eqs (1)–(3) the Kuhn-Tucker conditions

$$\lambda \geq 0, \quad F \leq 0, \quad \lambda F = 0 \tag{6}$$

must be fulfilled. To complete the rate boundary value problem we must specify the standard static and kinematic boundary conditions on complementary parts of the body surface S as well as the additional conditions for the plastic multiplier field on the boundary of the plastic part of the body V_λ. They can be derived from the variational principle for gradient plasticity by Mühlhaus et al. (1992) and have the form:

$$\delta \dot{\lambda} = 0 \quad \text{or} \quad (\nabla \dot{\lambda})^T v_\lambda = 0, \tag{7}$$

where δ denotes a variation of a quantity and v_λ denotes the outward normal to the elastic-plastic boundary.

The gradient dependence of the yield function makes the plastic consistency condition $\dot{F} = 0$ become a differential equation:

$$\left(\frac{\partial F}{\partial \sigma}\right)^T \dot{\sigma} + \frac{\partial F}{\partial \kappa} \dot{\kappa} + \frac{\partial F}{\partial \nabla^2 \kappa} \nabla^2 \dot{\kappa} = 0. \tag{8}$$

We introduce the gradient of the yield function $\mathbf{n}$:

$$\mathbf{n} = \frac{\partial F}{\partial \sigma}, \tag{9}$$

the (variable) hardening modulus h:

$$h(\kappa, \nabla^2 \kappa) = -\frac{\dot{\kappa}}{\dot{\lambda}} \frac{\partial F}{\partial \kappa}. \tag{10}$$

and the gradient influence variable g:

$$g(\kappa) = \frac{\dot{\kappa}}{\dot{\lambda}} \frac{\partial F}{\partial \nabla^2 \kappa}. \tag{11}$$

which is assumed to be a function of κ only. We limit our consideration to the theories of plastic flow, for which we can write that

$$\dot{\kappa} = \eta \dot{\lambda}, \tag{12}$$

73

with η constant and positive. This relation is broad enough to encompass the classical Huber-Mises, Drucker-Prager and Rankine yield functions with some form of a strain hardening hypothesis. We can now write eq. (8) in the form:

$$\mathbf{n}^T \dot{\sigma} - h\dot{\lambda} + g\nabla^2 \dot{\lambda} = 0 . \tag{13}$$

For softening the modulus h is negative and the additional variable g is positive. In the simplest case h and g are constants (softening is linear). For $g = 0$ the classical flow theory of plasticity is retrieved. The consistency condition is then a nonlinear algebraic equation, from which the plastic multiplier can be determined locally. The problem of solving eq. (13), which is valid in the plastic part of the body V_λ, is characteristic for the present theory.

Incremental formulation and algorithm

In this paper we employ a finite element discretization to solve simultaneously the two coupled equations of equilibrium and plastic consistency. For this purpose a weak satisfaction of the consistency condition is assumed and the plastic strain field is discretized in addition to the standard discretization of the displacements, Mühlhaus et al. (1991), de Borst et al. (1992). An incremental formulation of the boundary value problem gives rise to residual terms, which make a stress update necessary. In order to derive an incremental-iterative algorithm we require a weak satisfaction of the equilibrium condition

$$\int_V \delta\mathbf{u}^T (\mathbf{L}^T \sigma_{j+1} + \mathbf{b}_{j+1}) \, dV = 0 \tag{14}$$

and the yield condition

$$\int_{V_\lambda} \delta\lambda F (\sigma_{j+1}, \kappa_{j+1}, \nabla^2 \kappa_{j+1}) \, dV = 0 \tag{15}$$

at the end of iteration $j+1$ of the current loading step. These conditions lead to the following two integral equations, cf. Borst et al. (1992), Pamin (1994):

$$\int_V \delta\varepsilon^T \mathbf{D}^e (d\varepsilon - d\lambda\mathbf{m}) \, dV = \int_V \delta\mathbf{u}^T \mathbf{b}_{j+1} \, dV + \int_S \delta\mathbf{u}^T \mathbf{t}_{j+1} \, dS - \int_V \delta\varepsilon^T \sigma_j \, dV \tag{16}$$

and

$$\int_{V_\lambda} \delta\lambda \, [\mathbf{n}^T \mathbf{D}^e d\varepsilon - (h + \mathbf{n}^T \mathbf{D}^e \mathbf{m}) \, d\lambda + g\nabla^2 (d\lambda)] \, dV = -\int_{V_\lambda} \delta\lambda F (\sigma_j, \kappa_j, \nabla^2 \kappa_j) \, dV . \tag{17}$$

The values of $\mathbf{n}, \mathbf{m}, h$ and g on the left hand side of eq. (17) are determined at the end of iteration j, i.e. for the state defined by $(\sigma_j, \kappa_j, \nabla^2 \kappa_j)$. Using integration by parts for the last term on the left-hand side of eq. (17) we obtain

$$\int_{V_\lambda} \delta\lambda \, [\mathbf{n}^T \mathbf{D}^e d\varepsilon - (h + \mathbf{n}^T \mathbf{D}^e \mathbf{m}) \, d\lambda] \, dV - \int_{V_\lambda} g \, (\nabla\delta d\lambda)^T (\nabla d\lambda) \, dV = -\int_{V_\lambda} \delta\lambda F (\sigma_j + \kappa_j, \nabla^2 \kappa_j) \, dV, \tag{18}$$

provided the non-standard boundary conditions

$$\delta d\lambda = 0 \quad \text{or} \quad (\nabla d\lambda)^T v_\lambda = 0 \tag{19}$$

are fulfilled on the whole boundary S_λ of the plastic part of the body. The first condition is delicate for finite increments, since the elastic-plastic boundary moves when the plastic zone in the body evolves. During this process the boundary condition $\delta\lambda = 0$ on the momentary elastic-plastic boundary may be not true and $(19)_2$ must hold.

In the algorithm we enforce $F = 0$, $\mathbf{n} = \mathbf{m} = \mathbf{0}$ and $d\lambda = 0$ in the elastic part of the body and use the same mesh for both the equilibrium and failure condition, i.e. integrals over the whole volume V appear in eqs (15) and (17)/(18). In the residual terms on the right hand side of eqs (16) and (17)/(18) the stress σ_j appears. It is determined using the standard elastic predictor-plastic corrector algorithm (backward Euler type) at each integration point which is in a plastic state:

$$\sigma_j = \sigma_0 + \mathbf{D}^e \Delta\varepsilon_j - \Delta\lambda_j \mathbf{D}^e \mathbf{m}_j , \tag{20}$$

where σ_0 is the stress state at the end of the previous (converged) load increment and Δ denotes a total increment (from state 0 to iteration j). The values of κ_j and $\nabla^2\kappa_j$ are also updated using total increments. It is important to note that a consistent linearization is applied to this algorithm in order to derive a tangent operator used in the Newton-Raphson iterative procedure, cf. Pamin (1994). Since the vector $\mathbf{m}_j$ is known only after the mapping in eq. (20), it is approximated by the gradient $\mathbf{m}_t$ calculated for the "trial" stress:

$$\sigma_t = \sigma_0 + \mathbf{D}^e \Delta\varepsilon_j . \tag{21}$$

To decide whether an elastic point enters the plastic regime, or whether a plastic point begins elastic unloading the trial value of the yield function F_t is calculated at each integration point:

$$F_t = F(\sigma_t, \bar{\sigma}_g) , \tag{22}$$

where the gradient-dependent yield strength is determined as follows:

$$\bar{\sigma}_g = \bar{\sigma}(\kappa_j) - g(\kappa_j) \nabla^2\lambda_j . \tag{23}$$

An integration point is assumed to be in the plastic state when $F_t > 0$ and in the elastic state when $F_t < 0$. The gradient-dependent yield strength in eq. (23) is composed of two contributions. The gradient contribution $-g(\kappa)\nabla^2\lambda$ may be positive or negative. The former case occurs in the middle of the localization band, giving additional carrying capacity to the gradient-dependent material in this area (even if $\bar{\sigma}$ already equals zero, the yield strength $\bar{\sigma}_g$ is still larger than zero). The case of negative gradient contribution occurs at the elastic-plastic boundary, making it possible for the localization zone to spread (the elastic elements close to the elastic-plastic boundary have apparently a reduced yield strength). These modifications of the standard yield strength function $\bar{\sigma}(\kappa)$ are the algorithmic essence of the gradient regularization.

The dependence of the yield function on the Laplacian of the plastic strain measure is thus essential for the plastification condition and for the calculation of the non-standard residual forces on the

right hand side of eqs (17)/(18). To enable expansion of the plastic zone from the originally imperfect zones, the numerical solution must correctly determine a positive value of the Laplacian at the elastic-plastic boundary. The boundary conditions $(19)_2$ require the existence of derivatives of λ as nodal degrees of freedom. Therefore C^1-continuous interpolation functions are necessary for λ whether eq. (17) or eq. (18) is discretized, Pamin (1994).

Finite elements for gradient plasticity

C^1-formulation

In the integral equations (16) and (17)/(18) there appear at most first-order derivatives of the displacements and second-order derivatives of the plastic multiplier. Therefore, the discretization of the displacement field $\mathbf{u}$ requires C^0-continuous interpolation functions $\mathbf{N}$ and the discretization of the plastic multiplier λ requires C^1-continuous shape functions $\mathbf{h}$:

$$\mathbf{u} = \mathbf{Na}, \lambda = \mathbf{h}^T \Lambda , \tag{24}$$

where $\mathbf{a}$ is a nodal displacement vector and Λ denotes a vector of nodal degrees of freedom for the plastic multiplier field. The strain vector ε can then be written as

$$\varepsilon = \mathbf{Ba} , \tag{25}$$

where $\mathbf{B} = \mathbf{LN}$ according to the linear kinematic relation (2). The gradient of the plastic multiplier $\nabla \lambda$ and the Laplacian of the plastic multiplier $\nabla^2 \lambda$ are then discretized as follows:

$$\nabla \lambda = \mathbf{q}^T \Lambda, \quad \nabla^2 \lambda = \mathbf{p}^T \Lambda, \tag{26}$$

where $\mathbf{q}^T = \nabla \mathbf{h}^T$ and $\mathbf{p}$ contains the Laplacians of the interpolation functions in $\mathbf{h}$. Discretizing the integral equations (16) and (17) using eqs (24)–(26) and requiring that the result holds for all admissible $\delta \mathbf{a}$ and $\delta \Lambda$, one arrives at a nonlinear algebraic set of equations, de Borst et al. (1992):

$$\begin{bmatrix} \mathbf{K}_{aa} & \mathbf{K}_{a\lambda} \\ \mathbf{K}_{\lambda a} & \mathbf{K}_{\lambda \lambda} \end{bmatrix} \begin{bmatrix} d\mathbf{a} \\ d\Lambda \end{bmatrix} = \begin{bmatrix} \mathbf{f}_e + \mathbf{f}_a \\ \mathbf{f}_\lambda \end{bmatrix} , \tag{27}$$

with the classical elastic stiffness matrix $\mathbf{K}_{aa}$, the off-diagonal matrices

$$\mathbf{K}_{a\lambda} = -\int_V \mathbf{B}^T \mathbf{D}^e \mathbf{m} \mathbf{h}^T dV, \quad \mathbf{K}_{\lambda a} = -\int_V \mathbf{h} \mathbf{n}^T \mathbf{D}^e \mathbf{B} dV, \tag{28}$$

the gradient-dependent matrix

$$\mathbf{K}_{\lambda \lambda} = \int_V [(h + \mathbf{n}^T \mathbf{D}^e \mathbf{m}) \mathbf{h} \mathbf{h}^T - g \mathbf{h} \mathbf{p}^T] \, dV, \tag{29}$$

the classical external and internal force vectors $\mathbf{f}_e$ and $\mathbf{f}_a$, respectively, and the vector of residual forces emerging from the weak fulfilment of the yield condition:

$$\mathbf{f}_\lambda = \int_V F(\sigma_j, \lambda_j, \nabla^2 \lambda_j) \, \mathbf{h} \, dV. \tag{30}$$

The matrix $\mathbf{K}_{\lambda\lambda}$ is nonsymmetric due to the gradient dependence even for an associated flow rule. However, if eq. (18) is used as a point of departure instead of eq. (17) the matrix $\mathbf{K}_{\lambda\lambda}$:

$$\mathbf{K}_{\lambda\lambda} = -\int_V [\,(h + \mathbf{n}^T \mathbf{D}^e \mathbf{m}) \, \mathbf{h}\mathbf{h}^T - g\mathbf{q}\mathbf{q}^T\,] \, dV \tag{31}$$

becomes symmetric for associated plasticity ($\mathbf{m} = \mathbf{n}$).

With respect to the non-standard boundary conditions for the plastic multiplier field, we notice that both boundary conditions (19) are satisfied at the evolving elastic-plastic boundary if C^1-continuity is satisfied. However, the second of the conditions (19) must be enforced on the outer boundary of the plastic part or, in practice, on the whole surface of the body if the tangent operator in eq. (27) includes $\mathbf{K}_{\lambda\lambda}$ according to eq. (31) or if it does not possess a sufficient rank for elastic elements. To avoid singularity of the tangent operator for elastic elements the hardening modulus h in eq. (29) is initially set equal to Young's modulus E. The rank of submatrix $\mathbf{K}_{\lambda\lambda}$ for the elastic elements should be examined in order to determine the number of integration points and additional boundary conditions necessary to avoid spurious non-zero modes for the plastic multiplier field. On the other hand, a high-order integration scheme and too many additional boundary conditions for the λ field can lead to an overconstrained plastic flow and have a negative influence on the accuracy of finite element predictions, cf. Pamin (1994).

C^0-formulation

In order to be able to use C^0-continuous interpolation functions for the plastic multiplier field, we introduce new variables φ_x, φ_y :

$$\varphi_x = \frac{\partial \lambda}{\partial x}, \quad \varphi_y = \frac{\partial \lambda}{\partial y} \tag{32}$$

and collect them in a vector $\boldsymbol{\phi} = (\varphi_x, \varphi_y)$. In this fashion we can write the gradient of the plastic multiplier as

$$\nabla \lambda = \boldsymbol{\phi} \tag{33}$$

and represent the Laplacian of λ as

$$\nabla^2 \lambda = \frac{\partial \varphi_x}{\partial x} + \frac{\partial \varphi_y}{\partial y} = \nabla^T \boldsymbol{\phi}, \tag{34}$$

where the scalar product of the operator ∇^T and the vector field $\boldsymbol{\phi}$ denotes the divergence operator. The result of eq. (34) can be substituted in eq. (17) or (18), but the constraint (33) must be added to the formulation. We achieve this using the penalty method by means of an additional variational equation:

$$\int_V k (\nabla \lambda - \phi)^\mathsf{T} [\nabla (\delta \lambda) - \delta \phi] \, dV = 0 , \tag{35}$$

where k is a penalty factor. In practical calculations we use $k = E^3$, where E is Young's modulus. Using the incremental form of eq. (35) together with eqs (16) and (17) we obtain a set of three integral equations:

$$\int_V \delta \varepsilon^\mathsf{T} \mathbf{D}^e (d\varepsilon - d\lambda \mathbf{m}) \, dV = \int_S \delta \mathbf{u}^\mathsf{T} \mathbf{t}_{j+1} \, dS - \int_V \delta \varepsilon^\mathsf{T} \sigma_j \, dV, \tag{36}$$

$$\int_V \delta \lambda \, [\mathbf{n}^\mathsf{T} \mathbf{D}^e d\varepsilon - (h + \mathbf{n}^\mathsf{T} \mathbf{D}^e \mathbf{m}) \, d\lambda + g \nabla^\mathsf{T} d\phi] \, dV = -\int_V \delta \lambda F (\sigma_j, \kappa_j, \nabla^2 \kappa_j) \, dV, \tag{37}$$

where according to eqs (12) and (34) we calculate $\nabla^2 \kappa = \eta \nabla^\mathsf{T} \phi$ and

$$k \int_V \delta \lambda \nabla^\mathsf{T} [\nabla (d\lambda) - d\phi] \, dV - k \int_V \delta \phi^\mathsf{T} [\nabla (d\lambda) - d\phi] \, dV = 0 . \tag{38}$$

The above equations are now discretized using C^0-continuous interpolation functions. The interpolation functions for the displacement field are like in the previous section, but the shape functions $\mathbf{h}$ for the plastic multiplier field in eq. $(24)_2$ are now C^0-continuous. The following interpolation for the new variables in ϕ is used:

$$\phi = \mathbf{P}\Phi, \tag{39}$$

where Φ contains the nodal values of φ_x and φ_y and $\mathbf{P}$ is a matrix of shape functions, similar to $\mathbf{N}$ in eq. $(24)_1$. Upon the discretization of eqs (36–38) and the usual argument that the resulting equations must hold for any admissible $\delta \mathbf{a}$, $\delta \Lambda$ and $\delta \Phi$, we obtain the following set of algebraic equations in a matrix form:

$$\left\{ \begin{bmatrix} \mathbf{K}_{aa} & \mathbf{K}_{a\lambda} & \mathbf{0} \\ \mathbf{K}_{\lambda a} & \mathbf{K}_{\lambda \lambda} & \mathbf{K}_{\lambda \phi} \\ \mathbf{0} & \mathbf{0} & \mathbf{0} \end{bmatrix} + k \begin{bmatrix} \mathbf{0} & \mathbf{0} & \mathbf{0} \\ \mathbf{0} & \mathbf{K}^c_{\lambda \lambda} & \mathbf{K}^c_{\lambda \phi} \\ \mathbf{0} & \mathbf{K}^{cT}_{\lambda \phi} & \mathbf{K}^c_{\phi \phi} \end{bmatrix} \right\} \begin{bmatrix} d\mathbf{a} \\ d\Lambda \\ d\Phi \end{bmatrix} = \begin{bmatrix} \mathbf{f}_e + \mathbf{f}_a \\ \mathbf{f}_l \\ \mathbf{0} \end{bmatrix} \tag{40}$$

where $\mathbf{K}_{aa}$ is the classical elastic stiffness matrix, $\mathbf{K}_{a\lambda}$ and $\mathbf{K}_{\lambda a}$ are given in eq. (28), $\mathbf{K}_{\lambda \lambda}$ and $\mathbf{K}_{\lambda \phi}$ are defined as

$$\mathbf{K}_{\lambda \lambda} = \int_V (h + \mathbf{n}^\mathsf{T} \mathbf{D}^e \mathbf{m}) \mathbf{h} \mathbf{h}^\mathsf{T} dV, \quad \mathbf{K}_{\lambda \phi} = -\int_V [g \mathbf{h} \nabla^\mathsf{T} \mathbf{P}] \, dV, \tag{41}$$

and the submatrices with the superscript c in the additional (symmetric) matrix introducing the constraint (33) are defined as

$$\mathbf{K}^c_{\lambda \lambda} = \int_V \mathbf{q} \mathbf{q}^\mathsf{T} dV, \quad \mathbf{K}^c_{\phi \phi} = \int_V \mathbf{P}^\mathsf{T} \mathbf{P} dV, \quad \mathbf{K}^c_{\lambda \phi} = \int_V (-\mathbf{q} \mathbf{P}) \, dV. \tag{42}$$

The tangent operator in eq. (40) is again nonsymmetric, due to the gradient dependence.

78

If we substitute the definitions (33) and (34) into eq. (18), instead of into eq. (17), we obtain the weak form of the yield condition as:

$$\int_V \delta\lambda \, [\mathbf{n}^T \mathbf{D}^e \mathrm{d}\varepsilon - (h + \mathbf{n}^T \mathbf{D}^e \mathbf{m}) \, \mathrm{d}\lambda] \, \mathrm{d}V - \int_V g\,\delta\phi\mathrm{d}\phi\mathrm{d}V = -\int_V \delta\lambda F \, (\sigma_j, \kappa_j, \nabla^2 \kappa_j) \, \mathrm{d}V, \tag{43}$$

in which the derivatives of ϕ appear only on the right-hand side in $\nabla^2 \kappa_j$. Substitution of eqs (24)$_2$, (25) and (39) gives the second form of the discretized yield condition, which for an associated plastic flow ($\mathbf{m} = \mathbf{n}$) yields a symmetric tangent operator. The additional boundary conditions (19), written in the form:

$$\delta\mathrm{d}\lambda = 0 \quad \text{or} \quad \mathrm{d}\phi^T v_\lambda = 0 \tag{44}$$

must now be fulfilled on the boundary of the plastic part of the body.

We note that for the penalty method of introducing the constraint (33) to be successful the penalty submatrix $\mathbf{K}^c$ must be singular, otherwise non-zero Φ values are not admitted. To achieve this goal, reduced numerical integration should be used, cf. Zienkiewicz et al. (1982). Since the penalty constraint assures satisfaction of eq. (33) only in the sampling points, the best results are expected if uniformly reduced integration is employed for all the matrices. If eq. (33) is not true at a Gauss point, the stress computation gives a stress point that is not located on the yield surface and convergence is violated.

Requirements for the elements

Fig. 1 presents three examples of gradient plasticity elements. Element R32_G employs quadratic serendipity interpolation of displacements, bi-hermitian shape functions for the plastic strain field and 2×2 Gauss integration. This element is the most robust of gradient plasticity elements, cf. Pamin (1994), due to the special qualities of the Gauss integration stations, cf. Barlow (1976), at which higher-order accuracy of the derivatives of the interpolated fields is obtained and the yield condition is satisfied exactly upon convergence. As alluded to in the preceding, the matrix $\mathbf{K}_{\lambda\lambda}$ for elastic elements requires additional constraints, which can be introduced by extra boundary conditions for derivatives of λ. For an arbitrary assembly the conditions $\Lambda_n = 0$ and $\Lambda_{xy} = 0$ on the whole model boundary supply the required number of constraints. Element Q45_C is an example of a quadrilateral penalty-enhanced C^0-continuous element. With 2×2 integration it converges perfectly, but it possesses zero-energy modes for $\mathbf{u}$ and also spurious modes for λ. In an arbitrary mesh the boundary conditions for φ_x or φ_y are not sufficient to assure the correct rank of the $\mathbf{K}_{\lambda\lambda}$ matrix and additional conditions for λ itself on at least a part of the boundary are necessary to obtain a correct solution. The triangular element T21_G has quadratic interpolation of displacements and cubic interpolation of λ, which is based on a non-conforming plate bending triangle, cf. Zienkiewicz et al. (1991) . The element has Λ_x and Λ_y degrees of freedom, but it does not fulfil the continuity requirements for λ_n on its boundary. Integration with 3 Gauss points is used, but return mapping to the inside of the yield locus is observed and stress oscillations are found. Additional boundary conditions $\Lambda_n = 0$ are necessary to prevent the existence of non-zero λ modes in elastic elements. While testing different finite elements belonging to the described classes it was observed, cf. Pamin (1994), that for robustness the elements should fulfil some additional conditions:

79

- The balance of interpolations for displacements **u** and plastic multiplier λ. The best agreement is found between quadratic shape functions for **u** and cubic hermitian polynomials for λ or quadratic shape functions for λ and its derivatives.
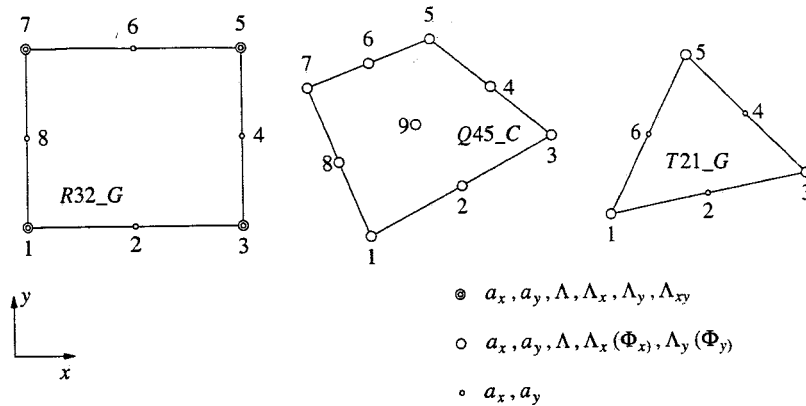

Fig. 1. *Gradient plasticity elements: C^1-continuous rectangle, C^0-continuous quadrilateral and non-conforming triangle.*

- The existence of a suitable integration quadrature. A sufficient number of integration points is necessary to prevent zero-energy modes for **u** and λ fields without introducing too many constraints and the sampling positions should be optimal for accuracy.
- The availability of additional boundary conditions for the λ field, necessary in combination with a symmetric tangent operator and helpful in removing spurious modes for the plastic multiplier field. The above discretization requirements favour the use of rectangular / quadrilateral elements with reduced integration. In fact, among the analyzed two-dimensional elements only the eight-noded serendipity / hermitian element *R32_G* fulfils all the requirements. Among the implemented triangular elements, the six-noded quadratic / non-conforming element *T21_G* with 3 integration points performs the best.

Application to geomechanics

Drucker-Prager gradient plasticity
The Drucker-Prager nonassociated plasticity model includes the hydrostatic stress dependence of the yield function and the non-normality of the plastic flow, which are characteristic for the behaviour of geomaterials. Assuming that the hardening / softening behaviour is limited to the cohesion of the material, the Drucker-Prager yield function for gradient-dependent plasticity can be written as follows:

$$F = \sqrt{3J_2} + \alpha p - \beta \bar{c}_g (\kappa, \nabla^2 \kappa), \tag{45}$$

where $p = \frac{1}{3}(\sigma_{xx} + \sigma_{yy} + \sigma_{zz})$ is the hydrostatic pressure, α and β are functions of the internal friction angle ϕ:

$$\alpha = \frac{6\sin\phi}{3-\sin\phi}, \quad \beta = \frac{6\cos\phi}{3-\sin\phi}, \tag{46}$$

and $\bar{c}_g$ is a gradient dependent measure of the cohesion. For non-associated plasticity we define the plastic potential function in a similar way:

$$G = \sqrt{3J_2} + \tilde{\alpha}p, \tag{47}$$

where $\tilde{\alpha}$ is a function of the dilatancy angle ψ similar to the definition of α in eq. (46). To determine the value of the constant η relating $\dot{\kappa}$ to $\dot{\lambda}$ according to eq. (12) we use the strain-hardening hypothesis:

$$\dot{\kappa} = \left(\frac{2}{3}\dot{\varepsilon}^p_{ij}\dot{\varepsilon}^p_{ij}\right)^{1/2}. \tag{48}$$

Substitution of the plastic strain rate vector $\dot{\varepsilon}^p = \dot{\lambda}\mathbf{m}$ into eq. (48) gives after some manipulations, cf. Pamin (1994):

$$\dot{\kappa} = \dot{\lambda}\left(1 + \frac{2}{9}\tilde{\alpha}^2\right)^{1/2}, \tag{49}$$

so that $\eta = \sqrt{1 + \frac{2}{9}\tilde{\alpha}^2}$. According to the definitions in eqs (10) and (11) we have:

$$h = \eta\beta\frac{\partial\bar{c}_g}{\partial\kappa}, \quad g = -\eta\beta\frac{\partial\bar{c}_g}{\partial\nabla^2\kappa}, \tag{50}$$

and for linear softening $\bar{c}_g$ can be written as:

$$\bar{c}_g = c_y + \frac{h}{\eta\beta}\kappa - \frac{g}{\eta\beta}\nabla^2\kappa, \tag{51}$$

with constant h and g. An important advantage of the Drucker-Prager yield function is its smoothness, since the presence of singular edges on the yield surface poses a difficulty for the gradient plasticity algorithm. In fact, the Drucker-Prager yield surface also possesses a vertex at the cross section with the hydrostatic axis $J_2 = 0$. From eq. (45) we can calculate that at the vertex $p = \bar{c}_g\cot\phi$. It is assumed here that the stress points in large triaxial tension, which would fall into the vertex regime $p > \bar{c}_g\cot\phi$, are not admitted.

Slope stability problem

Fig. 2 shows the configuration used for the analysis of stability of a soil mass under an increasing gravity load. It is a slope with an inclination of 45°, cf. Ortiz et al. (1987), for which the lower edge is fixed and the right edge is supported in the horizontal direction.

The material data are based on Ortiz et al. (1987): Young's modulus $E = 2 \cdot 10^8$ N/m^2, Poisson's ratio $v = 0.25$, initial cohesion $c_y = 2000$ N/m^2, friction angle $\phi = 20°$, dilatancy angle $\psi = 10°$. The soil density $\rho = 1000$ kg/m^3 is adopted. The linear softening rate for cohesion is $\partial\bar{c}/\partial\kappa = -0.01G$. From eq. (49) we obtain $\eta = \dot{\kappa}/\dot{\lambda} \approx 1.015$ and the softening modulus equals $h \approx -0.060G$ according to eq. (50)$_1$. The internal length scale $l = 0.04$ m is adopted (the gradient constant is $g \approx 2752$ N). In this example we employ two crossed-diagonal meshes with $12 \times 12 \times 4$ and $24 \times 24 \times 4$ six-noded plane strain triangles T21EG with 3 integration points. Along all the boundaries the normal derivatives of

the plastic multiplier Λ_n are set to zero. The calculations are performed under arc-length or single displacement control. In the latter case the vertical displacement of point A is the controlling parameter (cf. Fig. 2).
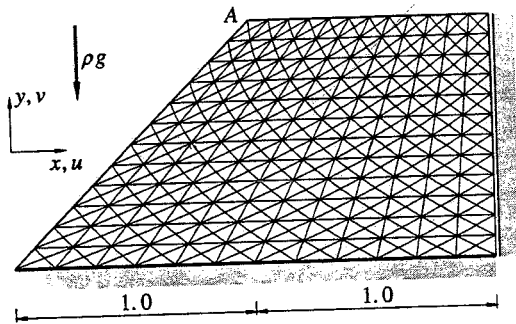

Fig. 2. Inclined embankment model (dimensions in m).

In addition to the linear softening case we consider the ideal plasticity case $\partial \bar{c} / \partial \kappa = 0$. In the gradient plasticity calculations the coefficient $g = 2752\ N$ is used. Fig. 3 presents the load-displacement diagrams. With the increase of the self-weight (at the load factor value 1.8) the compressed soil mass starts to plastify at the bottom of the embankment. The plastic zone then gradually expands upwards and at the peak load a shear band forms, along which a part of the soil mass slides down.
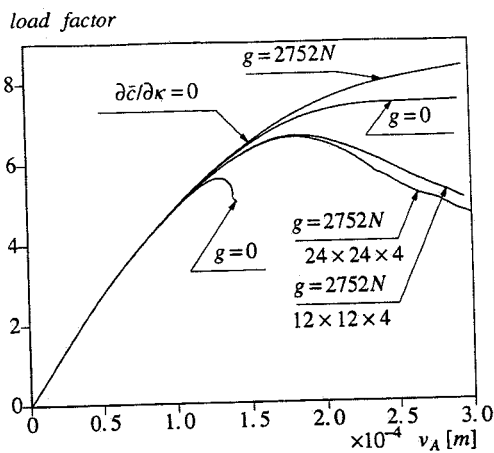

Fig. 3. Classical versus gradient plasticity solutions for the slope stability problem in terms of gravity load factor and vertical displacement at point A.

Calculations for the classical softening plasticity case fail soon after the formation of the shear band. The gradient plasticity algorithm gives a more stable behaviour, the peak load is higher and the response is more ductile. The results for both analyzed meshes are close, but not the same (Fig. 3) since the non-conforming triangular elements $T21EG$ does not fulfil the robustness requirements. Fig. 4 compares the contour plots of the equivalent plastic strain obtained for the two analyzed

discretizations. The expected smoothing effect is observed and the curved shear band has the width of several elements. The strains are slightly more localized for the fine mesh, but the shear band width is well reproduced.
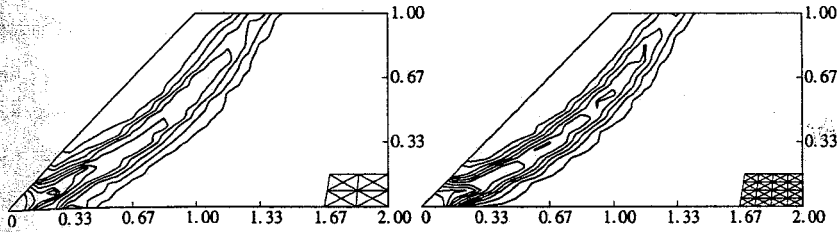

Fig. 4. Contour plots of equivalent plastic strain for two discretizations (l = 0.04 m).

For the ideal plasticity case the gradient dependence produces an increased load carrying capacity (Fig. 3) and a broader shear band is observed. In fact, the relation between the coefficient g, which scales the gradient influence, and the internal length l (hence also the shear band width) is not determined in this case, which corresponds to the gradual increase of the shear band width, observed in the incremental solution.

Application to concrete fracture

Vertex-enhanced Rankine gradient plasticity

The maximum principal stress criterion, adopted as a condition of continuum fracture, is formulated here for the plane stress case. A similar form of the yield criterion can be assumed for plane strain situations provided we assure that $\sigma_3 = \sigma_z < \bar{\sigma}_g$ (or σ_y), which means that cracking is admitted only in planes parallel to the z-axis. The Rankine failure function can be written in the following form:

$$F = \sigma_1 - \bar{\sigma}_g \, (\kappa, \nabla^2 \kappa),$$ (52)

where σ_1 is the maximum principal stress and $\bar{\sigma}_g$ is the gradient dependent fracture strength. For this fracture criterion the following definition of the equivalent inelastic strain rate is proposed:

$$\dot{\kappa} = \left| \dot{\varepsilon}_1^p \right|,$$ (53)

where $\dot{\varepsilon}_1^p$ is the maximum principal inelastic strain rate. Substitution of the associated flow rule $\dot{\varepsilon}^p = \dot{\lambda} \mathbf{n}$ into eq. (53) gives after some manipulations, cf. Pamin (1994):

$$\dot{\varepsilon}_1^p = \dot{\lambda} .$$ (54)

We assume that the Rankine yield criterion is activated only when σ_1 and $\dot{\varepsilon}_1^p$ are positive, so that we obtain the equivalence the inelastic strain measure and the plastic multiplier $\dot{\kappa} = \dot{\lambda}$.

83

The Rankine yield surface for plane stress problems possesses a vertex $\sigma_v = (\bar{\sigma}, \bar{\sigma}, 0)$ in the $(\sigma_x, \sigma_y, \sigma_{xy})$ space. For classical plasticity algorithms the presence of vertices in yield functions involves only some extra difficulties, cf. de Borst (1987), Simo et al. (1988). Each smooth part of the yield function can first be redefined as a separate function (for instance $F_{(1)}$ and $F_{(2)}$) and then the Koiter's generalization can be applied, Koiter (1953).

The situation is different if, as in gradient plasticity algorithm, the plastic multiplier is discretized and the yield condition is fulfilled in a weak sense. A possible, but expensive solution (following the Koiter's strategy) is to include the discretization of two plastic multipliers $\lambda_{(1)}$ and $\lambda_{(2)}$ in the element formulation and penalize the latter one to zero, unless the vertex regime is entered. The second approach, summarized below, is to apply a smooth approximation of the Rankine yield function, cf. Pamin (1994).

For vertex smoothing we develop a family of yield functions in the two-dimensional principal stress space, tangential to the Rankine function in the points $(0, \bar{\sigma})$ and $(\bar{\sigma}, 0)$:

$$F_m = (\sigma_1^m + \sigma_2^m)^{1/m} - \bar{\sigma}_g = 0 . \tag{55}$$

In fact, these yield surfaces are not fully compatible with the Rankine yield surface in the $(\sigma_x, \sigma_y, \sigma_{xy})$ space, a growing incompatibility exists along the lines $\sigma_x = 0$ and $\sigma_y = 0$ as σ_{xy} increases. However, assuming that the enhanced Rankine criterion will be active for stress states dominated by tension and not by shear, the yield function F_2 according to eq. (55) is adopted henceforth. A modified strain-hardening hypothesis:

$$\dot{\kappa} = \left[(\dot{\varepsilon}_1^p)^2 + (\dot{\varepsilon}_2^p)^2 \right]^{1/2} \tag{56}$$

assures the equivalence the plastic strain measure and the plastic multiplier $\dot{\kappa} = \dot{\lambda}$.

We employ a nonlinear softening rule according to eq. (23):

$$\bar{\sigma}_g (\kappa, \nabla^2 \kappa) = \bar{\sigma}(\kappa) - g(\kappa) \nabla^2 \kappa, \tag{57}$$

in which $\bar{\sigma}(\kappa)$ is a given softening rule (e.g. as in Fig. 5), $g(\kappa)$ is a given gradient influence function and we assume that $\bar{\sigma}_g \geq 0$. We can generalize the relation between the variable g, the classical hardening modulus $\bar{\sigma}'$ and an internal length scale l, found for the one-dimensional analytical solution and linear softening, de Borst et al. (1992), to the case of nonlinear softening

$$g(\kappa) = -l^2 \bar{\sigma}'(\kappa), \tag{58}$$

with l constant, and obtain for the gradient-dependent softening law:

$$\bar{\sigma}_g (\kappa, \nabla^2 \kappa) = \bar{\sigma}(\kappa) - l^2 \bar{\sigma}'(\kappa) \nabla^2 \kappa, \tag{59}$$

which together with the exponential softening rule in Fig. 5 reflects the decrease of the gradient influence with the increase of the accumulated plastic (inelastic) strain, corresponding to the gradual failure of microstructural deformation carriers during a progressive material damage, van Mier (1991).
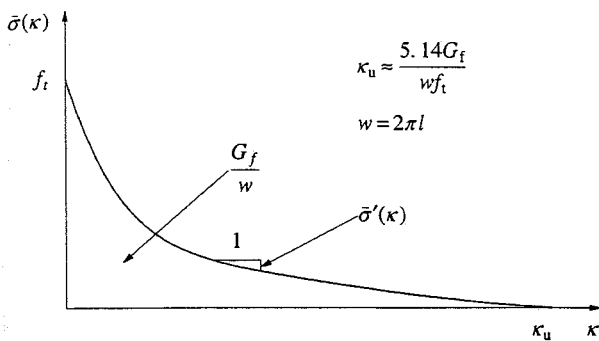
$$\kappa_u \approx \frac{5.14 G_f}{w f_t}$$

$$w = 2\pi l$$

Fig. 5. *Nonlinear softening rule for concrete Mode-1 fracture according to Hordijk (1991).*

Single-edge-notched beam

The single-edge-notched beam in Fig. 6 has been investigated by Schlangen (1993) experimentally and numerically using a lattice model. The beam has a 5 mm wide and 20 mm deep notch on the symmetry axis at the top and is subjected to an antisymmetric loading.
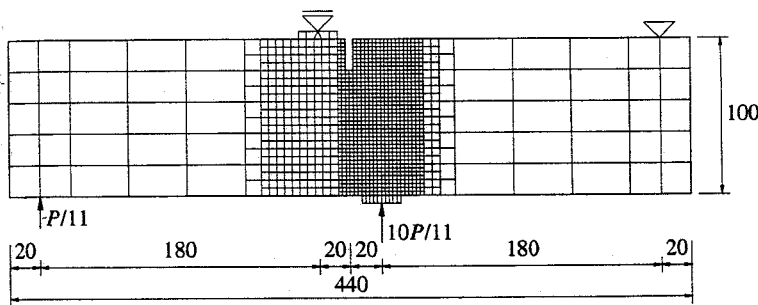

Fig. 6. *Single-edge-notched beam with discretization (dimensions in mm).*

The material data for concrete, based on experimental values, cf. Schlangen (1993), are as follows: Young's modulus $E = 35000$ N/mm^2, tensile strength $f_t = 3.00$ N/mm^2, fracture energy $G_f = 0.10$ N/mm. To preserve the robustness of the Rankine gradient plasticity algorithm with vertex smoothing the Poisson ratio equal to zero is taken, which, for the plane stress configuration, involves a negligible deviation of results with respect to the real case with $v = 0.2$. The beam is analyzed numerically under indirect arc length control.

Since fracture takes place in the middle of the beam, the element mesh (Fig. 6) is composed of the following parts:

− the middle zone (115 × 100 mm) with a "real" notch, discretized using eight-noded gradient plasticity elements *R32MG*; the additional boundary conditions for the plastic multiplier λ are imposed on the boundaries of this zone,

− two coarse mesh zones of standard eight-noded elements on both sides of the beam,

− the loading plates discretized with standard quadrilateral and triangular elements having ten times higher stiffness $E = 350000$ N/mm^2.

The nonlinear softening rule and the decreasing gradient influence according to eq. (59) are used. In the first simulation an internal length scale $l = 3$ mm ($\kappa_u = 9.09 \cdot 10^{-3}$) is assumed, then $l = 2$ mm ($\kappa_u = 0.0136$) is taken. In the third simulation the fracture energy is doubled to observe its influence on the peak load and ductility of the response ($l = 3$ mm is adopted). To study the mesh-sensitivity and to check whether the curved crack obtained in experiments can be reproduced, the mesh in the central area (50×100 mm) is refined uniformly in the fourth simulation.

Fig. 7 shows load-crackmouth sliding displacement (CMSD) diagrams for the experiment of Schlangen (1993) and the four cases. The global behaviour of the beam is reproduced satisfactorily with the Rankine gradient plasticity model, Mode-I crack opening is observed and the simulation results are close to the experiment. For $G_f = 0.1$ N/mm three curves are shown: for the two meshes with $l = 2$ mm and for the coarser mesh with $l = 3$ mm. The load-deformation diagram is governed by the value of the fracture energy and it is almost not affected by either mesh refinement or the change of the internal length scale. Fig. 8 presents the expected regularization effect: the fracture is distributed over a band having a width determined by the internal length scale. The equal value contours for the equivalent fracture strain are similar for the two used meshes. At the same time the experimental propagation of the primary crack along a curved line is not reproduced.

While the present solution algorithm for gradient plasticity performs very well for relatively smooth strain/stress fields, the return mapping determined by the nodal plastic multiplier variables is not sufficiently accurate in case of stress concentrations (e.g. at notches) and sudden changes of the plastic flow direction (e.g. when the vertex regime of the Rankine criterion is entered).

This difficulty, which is a consequence of the weak fulfilment of the yield condition, causes convergence problems especially in the peak load regime.
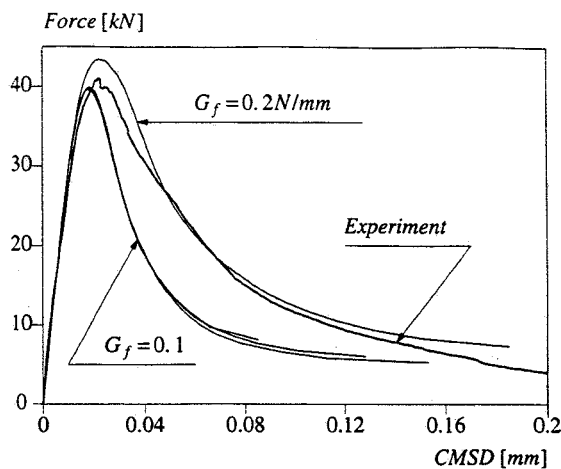

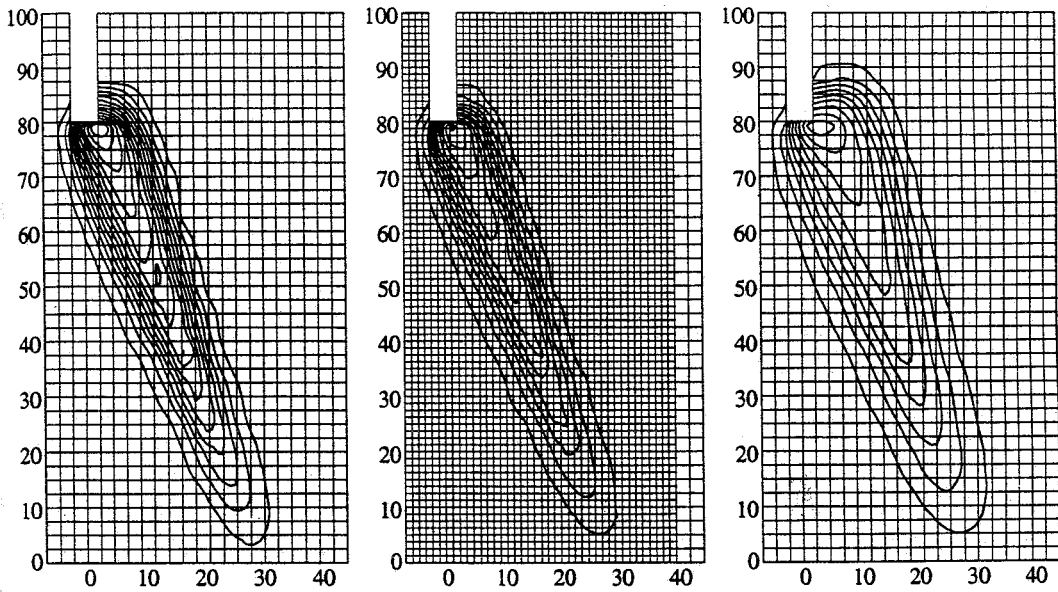Fig. 7. Computed and experimentally obtained load-CMSD diagrams.

Fig. 8. Contour plots of equivalent fracture strain in the central part of the SEN beam at the final load level:
l = 2 mm (left and middle) and l = 3 mm (right).

Double-edge-notched specimen

Fig. 9 shows the configuration of a mixed-mode concrete fracture test, analyzed experimentally by Nooru-Mohamed (1992). The double-edge-notched specimen was placed in a special loading frame that allowed for the analysis of various loading paths of combined shear and tension under force or deformation control.
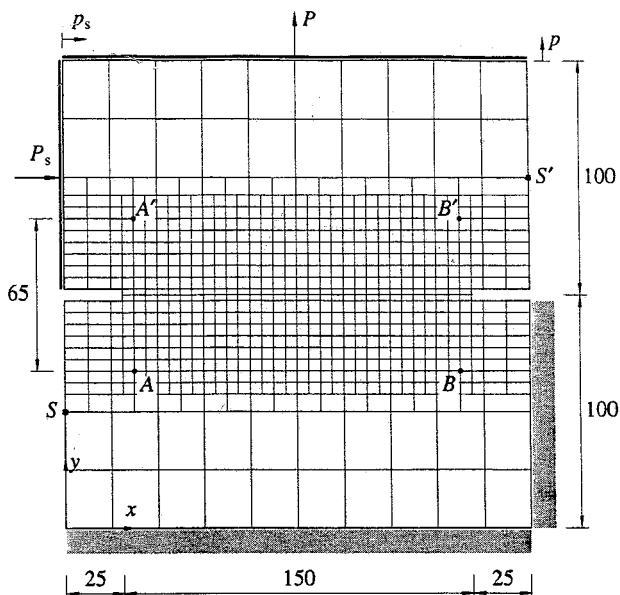

Fig. 9. Double-edge-notched concrete specimen with discretization (dimensions in mm).

Three specimen sizes ($L \times L$) were used in the experiments: 200×200, 100×100, 50×50 mm. The sizes of symmetrical notches were 25×5, 12.5×5 and 6.25×5 mm, respectively, and the specimen thickness was for all cases $t = 50$ mm. The specimen was supported at the bottom and along the right-hand side below the notch. The shear force P_s was applied through the frame above the notch along the left-hand side of the specimen and the tensile force P was applied at the top. The frames were glued to the specimen. The relative shear deformation between the upper and lower half of the specimen δ_s was measured at the points S and S' on both sides and the relative normal deformation in the fracture zone δ was measured between the points A and A' as well as B and B' and averaged. Owing to the servo-controlled system the loading could also be controlled by the deformations δ_s and δ.

We have analyzed two of the loading paths considered by Nooru-Mohamed (1992) using the Rankine gradient dependent plasticity model. In the first series of simulations the largest specimen is used. The shear force is applied under force control and then kept constant while the normal loading is imposed under deformation control of δ (path 4 from the experiment). In the second series all three sizes are analyzed to verify the size effect, which is a result of the release of the stored elastic energy during fracture. To obtain a monotonic increase of loading, the shear and tension are applied simultaneously under the control of the horizontal and vertical displacements p_s and p with the condition $p = p_s$. It is noted that this deformation control is only a numerically convenient approximation of the real case, since in the experiment (path 6) δ_s and δ were used to control the loading. The material data used in numerical simulations are as follows: Young's modulus $E = 30000$ N/mm^2, Poisson's ratio $v = 0.0$, tensile strength $f_t = 0.8 f_{spl} \approx 3.00$ N/mm^2, fracture energy $G_f = 0.10$ N/mm. The same nonlinear softening rule as in the previous section is employed. Unless stated otherwise, the internal length scale $l = 2$ mm ($\kappa_u = 0.0136$) is assumed.

Fig. 9 shows the geometry of the specimen 200×200 mm and the finite element mesh used in the calculations. The central zone of refined mesh ($50 \leq y \leq 150$) is composed of eight-noded gradient plasticity elements R32MG and the coarse mesh zones at the top and at the bottom are discretized with standard serendipity elements. Additional boundary conditions for the plastic multiplier field are enforced on the boundaries of the fine mesh and the respective displacements are tied on the remeshing lines to preserve the displacement continuity.

Fig. 10 shows the experimentally determined and numerically simulated relations between the tensile load P and the normal displacement δ. The calculated maximum shear load $P_{s\,max} = 29.7$ kN islarger than the experimental value (about 27.5 kN) and the ultimate carrying capacity under subsequent tension is even stronger overestimated, which is attributed to the stress locking in the notch area and overestimation of the cracking stress in the presence of the lateral compression. On the other hand, the Rankine gradient plasticity model reproduces correctly the character of the experimental curves and is close to experiments for progressive softening.

The simulated fracture process zones are compared in Fig. 11 with the average experimental crack positions, i.e. an average of the experimental crack locations at the front and back of the specimen are plotted. The agreement is reasonable and no bias of the mesh lines is found as was the case in the smeared cracking simulations, cf. Nooru-Mohamed (1992). It is noted that for the case with $P_{s\,max}$ the central zone of gradient plasticity elements had to be extended over the area $40 \leq y \leq 160$ in order to admit the inclined "crack" propagation. For the case $P_s = 5$ kN two fracture zones developing

from the notches finally join, for the other cases the width of the compressive strut is estimated correctly. The width of the fracture zones corresponds well to the assumed value $w = 2\pi l \approx 12.6$ mm. However, as for the SEN beam in the previous section, the curved character of the cracks cannot be simulated.
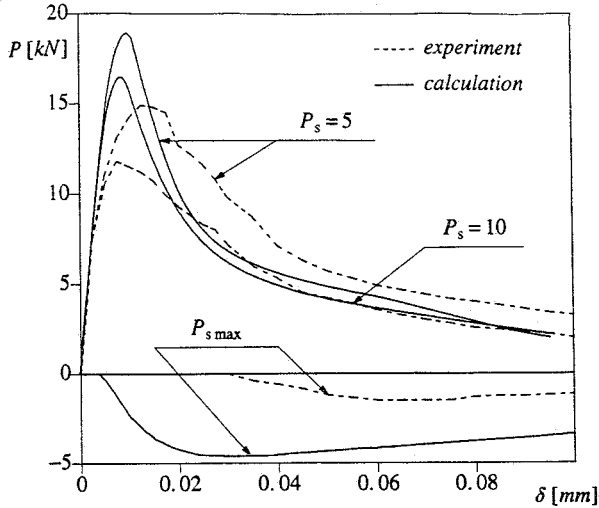

Fig. 10. Computed and experimental tensile force versus average normal displacement diagrams (path 4).
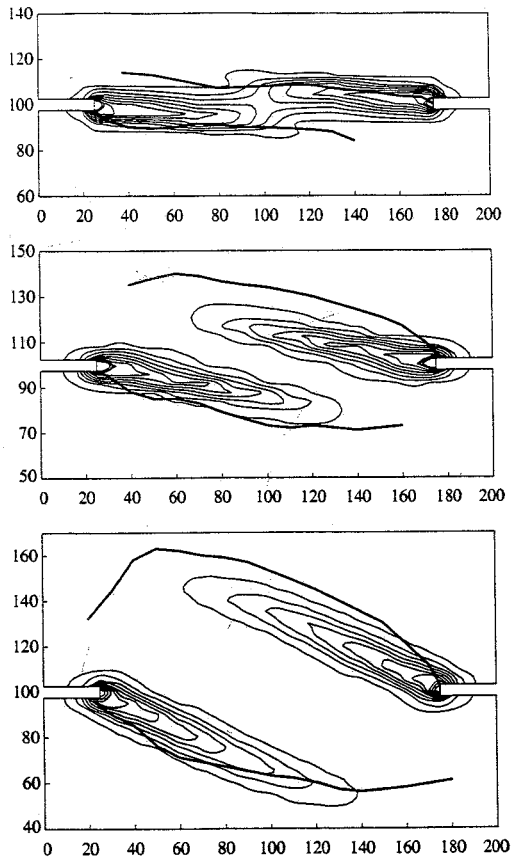

Fig. 11. Contour plots of equivalent fracture strain at the final tensile load level for the three lateral confining load levels (from the top $P_s = 5, 10, P_{s\,max}$).

In the second series of calculations we have applied simultaneously equal shear and tensile deformation (path 6). Fig. 12 shows the calculated diagrams for the relation between the nominal stress $(P/(tL_0))$, where L_0 is the load carrying length equal to 150, 75 and 37.5 mm for the three respective specimen sizes, and the average normal strain (δ/L). For the smaller specimens two possibilities are considered: a changing internal length $l = 1/0.5$ mm (so that $l/L = 0.01$) and a constant internal length $l = 2$ mm. For all cases the fracture energy G_f is the same.
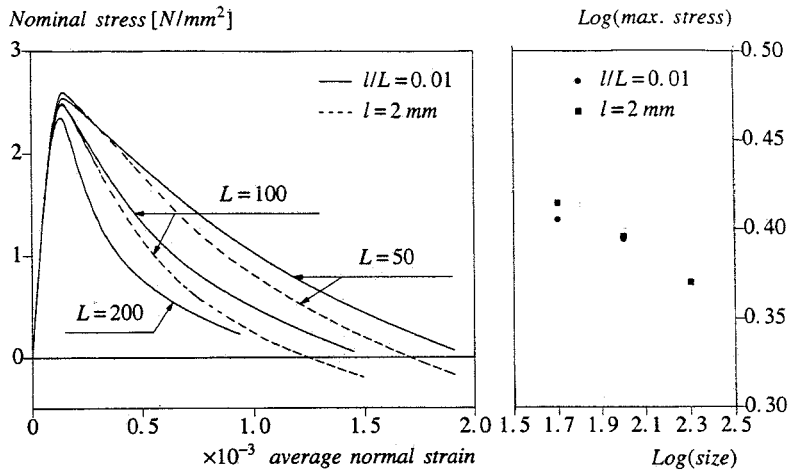

Fig. 12. Nominal tensile stress versus average tensile strain diagram and the size effect on the peak-stress (path 6).

As can be seen in Fig. 13 the choice of the internal length can influence the predicted fracture mode. If the internal length scale is decreased together with the specimen size, two cracks are predicted for all three specimens. If the internal length is kept constant, we find just one fracture zone for the medium and small specimen. It is noted that in the experiments both crack patterns, distributed and with dominant cracks, were observed in the series of medium and small specimens. From Fig. 12 we observe, that the choice of the internal length influences the softening behaviour. A classical size effect is found both in the peak-stress value and the post-peak regime although in the experiment a reversed size effect was found for path-6 tests. It is mentioned that since an internal length scale is incorporated in the numerical model, the predicted size effect law need not be a power law and our results correspond to the predictions of nonlinear elastic fracture mechanics, cf. Bažant (1992).
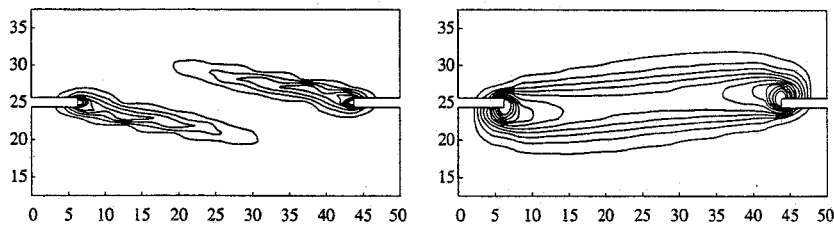

Fig. 13. Contour plots of equivalent fracture strain for the smallest specimen and different internal length values: l = 0.5 mm (left and l = 2mm (right).

90

In sum, the gradient-dependent Rankine plasticity model seems to be less accurate for the mixed-mode fracture problem than for the plain Mode-I cases. As in the SEN beam example the curved shape of the experimentally observed cracks has not been reproduced. However, the localization limiting properties of gradient plasticity make the results much closer to experiments than the results of the smeared-cracking model, cf. Nooru-Mohamed (1992).

Final remarks

In this paper the potential of gradient-dependent plasticity, Mühlhaus et al. (1991), de Borst et al. (1992) as a localization limiter in shear (Mode-II), tension (Mode-I) and mixed mode problems has been assessed. The employed continuum theory includes a regularizing dependence of the yield function on higher-order spatial derivatives of a plastic strain measure and therefore the boundary value problem for a softening continuum remains well-posed in the post-peak regime.

The fundamental feature of the used algorithm is a weak (and not pointwise) satisfaction of the yield condition, which is coupled with a weak equilibrium condition. The dependence of the yield function on the Laplacian of the plastic strain measure induces the necessity of C^1-continuous interpolation of the plastic strain field in the incremental formulation. However, a C^0-approach has also been presented, in which the continuity requirement is relaxed by treating the first derivatives of the plastic multiplier as additional unknowns and connecting them to the plastic multiplier field using a penalty constraint.

Most of the implemented elements introduce properly the localization limiting properties of the gradient-dependent continuum: the results of finite element simulations are almost insensitive to mesh refinement or alignment, since the width of the shear bands (fracture process zones) is determined by the internal length scale incorporated in the theory.

The problems solved prove that the gradient plasticity models may be successfully applied in the numerical verification of experiments as well as the simulation of instability phenomena in frictional materials. The approach is effective for the description of localized failure under Mode-I, Mode-II and mixed-mode conditions.

A vertex-enhancement of the Rankine criterion is required for a proper modelling of Mode-I and mixed mode fracture of concrete. Though no fully robust solution has been found within the frame of the present algorithm, acceptable results have been obtained when the vertex is smoothed. The Rankine softening gradient plasticity with an exponential softening rule and a decreasing gradient influence reproduces closely the experimentally observed structural response and size effect. The load-deformation diagrams for these problems are governed by the value of fracture energy G_f and are not affected by the assumed value of the internal length, unless its change results in a different localization mode.

Acknowledgements

References

AIFANTIS E.C. (1984), On the microstructural origin of certain inelastic models, *J. Eng. Mater. Technol.*, **106**, pp. 326–330.

BARLOW J. (1976), Optimal stress locations in finite element model, *Int. J. Num. Meth. Eng.*, **10**, pp. 243–251.

BAŽANT Z.P. (1992), Scaling laws in mechanics of failure, *ASCE J. Eng. Mech.*, **119**, pp. 1828–1845.

DE BORST R. (1987), Integration of plasticity equations for singular yield functions, *Comp. & Struct.*, **26**, pp. 823–829.

DE BORST R. and MÜHLHAUS H.-B. (1992), Gradient-dependent plasticity: Formulation and algorithmic aspects, *Int. J. Num. Meth. Eng.*, **35**, pp. 521–539.

DE BORST R., SLUYS L.J., MÜHLHAUS H.-B., PAMIN J. (1993), Fundamental issues in finite element analyses of localization of deformation, *Eng. Comput.*, **10**, pp. 99–121.

HORDIJK D.A. (1991), *Local approach to fatigue of concrete*, Dissertation, Delft University of Technology, Delft.

KOITER W.T. (1953), Stress-strain relations, uniqueness and variational theorems for elastic-plastic materials with a singular yield surface, *Q. Appl. Mech.*, **11**, pp. 350–354.

VAN MIER J.G.M. (1991), Mode-I fracture of concrete: discontinuous crack growth and crack interface grain bridging, *Cement and Concrete Research*, **21**, pp. 1–15.

MÜHLHAUS H.-B. and AIFANTIS E.C. (1991), A variational principle for gradient plasticity, *Int. J. Solids Structures*, **28**, pp. 845–857.

NOORU-MOHAMED M.B. (1992), *Mixed-mode fracture of concrete: an experimental approach*, Dissertation, Delft University of Technology, Delft.

ORTIZ M., LEROY Y. and NEEDLEMAN A. (1987), A finite element method for localized failure analysis, *Comp. Meth. Appl. Mech. Eng.*, **61**, pp. 189–214.

PAMIN J. (1994), *Gradient-dependent plasticity in numerical simulation of localization phenomena*, Dissertation, Delft University of Technology, Delft.

SCHLANGEN E. (1993), *Experimental and numerical analysis of fracture processes in concrete*, Dissertation, Delft University of Technology, Delft.

SIMO J.C., KENNEDY J.G. and GOVINDJEE S. (1988), Non-smooth multisurface plasticity and viscoplasticity. Loading/unloading conditions and numerical algorithms, *Int. J. Num. Meth. Eng.*, **26**, pp. 2161–2185.

SLUYS L.J. (1992), *Wave propagation, localization and dispersion in softening solids*, Dissertation, Delft University of Technology, Delft.

VARDOULAKIS I. and AIFANTIS E.C. (1991), A gradient flow theory of plasticity for granular materials, *Acta Mechanica*, **87**, pp. 197–217.

WILLAM K.J. and DIETSCHE A. (1992), Fundamental aspects of strain-softening descriptions, *Fracture Mechanics of Concrete Structures*, Ed. Z.P. Bažant, Elsevier Applied Science, London and New York, pp. 227–230.

ZBIB H.M. and AIFANTIS E.C. (1988), On the localization and postlocalization behavior of plastic deformation, I,II,III, *Res Mechanica*, **23**, pp. 261–277, 279–292, 293–305.

ZIENKIEWICZ O.C. and NAKAZAWA S. (1982), The penalty function and its applications to the numerical solution of boundary value problems, *Am. Soc. Mech. Eng. AMD*, **51**, 22 pp. 157–179.

ZIENKIEWICZ O.C. and TAYLOR R.L. (1991), *The Finite Element Method, Fourth Edition*, Vol.2, Chapter 1–2, McGraw-Hill, London.